Effect of duty cycle and electrolyte additive on photocatalytic performance of TiO2-ZrO2 composite layers prepared on CP Ti by micro arc oxidation method

Document Version
Accepted author manuscript

Link to publication record in Manchester Research Explorer

Citation for published version (APA):
Babaei, M., Dehghanian, C., Taheri, P., & Babaei, M. (2016). Effect of duty cycle and electrolyte additive on photocatalytic performance of TiO_2-ZrO_2 composite layers prepared on CP Ti by micro arc oxidation method. *Surface and Coatings Technology*, *307*, 554-564. https://doi.org/10.1016/j.surfcoat.2016.09.050

Published in:
Surface and Coatings Technology

Accepted Manuscript

Effect of duty cycle and electrolyte additive on photocatalytic performance of TiO$_2$-ZrO$_2$ composite layers prepared on CP Ti by micro arc oxidation method

Mahdi Babaei, Changiz Dehghanian, Peyman Taheri, Masoud Babaei

Please cite this article as: Mahdi Babaei, Changiz Dehghanian, Peyman Taheri, Masoud Babaei, Effect of duty cycle and electrolyte additive on photocatalytic performance of TiO$_2$-ZrO$_2$ composite layers prepared on CP Ti by micro arc oxidation method, *Surface & Coatings Technology* (2016), doi: 10.1016/j.surfcoat.2016.09.050

Effect of duty cycle and electrolyte additive on photocatalytic performance of TiO₂-ZrO₂ composite layers prepared on CP Ti by micro arc oxidation method

Mahdi Babaei[a], Changiz Dehghanian[a1], Peyman Taheri[b], Masoud Babaei[c]

a.   *School of Metallurgy and Materials Engineering, College of Engineering, University of Tehran, Tehran, Iran*

b.   *Electrical Engineering and Computer Sciences, University of California, Berkeley, California 94720, United States*

c.   *School of Chemical Engineering and Analytical Science, University of Manchester, Manchester, United Kingdom*

[1] Corresponding author

E-mail address: cdehghan@ut.ac.ir (C. Dehghanian).

1

Abstract

The aim of this work is to discuss the photocatalytic performance of the titania-zirconia porous photocatalyst layers synthesized via micro arc oxidation technique. An attempt was also made to put forward the basic formation mechanism of the layers. Impedance and optical properties of the photocatalyst layers were studied by electrochemical impedance spectroscopy (EIS), Photoluminescence spectroscopy and UV–vis absorption spectroscopy, in order to assess their intrinsic catalytic properties. The results of the EIS were correlated with the microstructural characteristics along with measurements of Methylene Blue (MB) photocatalytic degradation. The results show enhanced photocatalytic activity of TiO_2-ZrO_2 composite layers compared to pure TiO_2 layer. It was revealed that the photocatalytic activity of the layers prepared at different duty cycles is influenced by characteristics of microdischarge regime imposed by working electrolytes with varying additive concentration. The results of photocatalytic degradation of methylene blue were in good agreement with those obtained from electrochemical analysis.

Keywords: TiO_2-ZrO_2; Micro arc oxidation; Photocatalyst; Methylene blue.

1. Introduction

Among the various photocatalysts, titanium dioxide (TiO_2) has received much attention due to its high photocatalytic activity, thermal stability and non-corrosive properties, biological and chemical inertness [1]. Considering the wide band gap between its valence and conduction bands, there would be a strong oxidizing power to create •OH radicals and reduction of oxygen molecules absorption on the surface, making it a promising photocatalyst able to decompose most organic pollutants [2, 3]. Nevertheless, the applications of pure TiO_2 are limited due to the high electron-hole pair recombination rate and low efficiency of visible light utilization arising from its wide band gap which means that it can be only excited under UV light wavelength. Hence, considerable efforts have been focused on increasing the ability of a photocatalytic material to overcome charge recombination and allow separated charges to interact with molecules at the surface of the material (photocatalytic efficiency). Several modifications have been employed for improving the charge separation efficiency of TiO_2 such as doping titania with noble metals [4, 5], metal ions [6-8] or incorporation of other semiconductor metal oxide [9]. The incorporating metal ions into TiO_2 is considered an efficient approach for acquiring an improved photocatalyst by introducing intermediate impurity energy levels, allowing the CB electrons to flow to noble metals and escape from recombination [10-12].

ZrO_2 is an n-type semiconductor that exhibits high ion exchange capacity and redox activities along with comparable physic-chemical properties to TiO_2. Benefitting from wide band gap ($\sim$5.0 eV) alongside conduction and valence bands with more-negative (-1.0 V vs NHE) and more-positive (4.0 V vs NHE) reducing potentials respectively, ZrO_2 is expected to be an efficient support catalyst for TiO_2 in photo-degradation application [13, 14]. ZrO_2–TiO_2 binary oxide catalysts have stood out as potential materials comprehensively used in the field of heterogeneous catalysis and sensor technology due to their good optical and electronic properties and photo-stability [15, 16]. Recently, it has been found that ZrO_2–TiO_2 composite photocatalysts [17, 18] display enhanced photochemical properties (both in gas and aqueous

3

solutions) than pure TiO_2 which mostly results from improved photo-generated electrons and holes separation owing to the synergistic effect of two semiconductor materials under the light function. It was also reported that the trapping of abundant OH groups on the surface of binary oxide catalyst by holes promotes the suppression of the recombination process which, in turn, improves the quantum efficiency. It is also demonstrated that incorporation of ZrO_2 in TiO_2 can promote the thermal stability of the catalyst by preventing the phase transformation from anatase to rutile [19-21].

Typically, ZrO_2–TiO_2 composites have been synthesized via different methods including co-precipitation, sol–gel process, evaporation-induced self-assembly, and microwave-assisted solution combustion method. Micro arc oxidation (MAO) method is an economic, environmentally benign and one-step process with short working time. During MAO process discharge channels formed by electrical sparks with local temperature and pressure reaching 10^3 to 10^4 K and 10^2 to 10^3 MPa, respectively, give rise to plasma thermochemical interactions between the substrate and the electrolyte species and let the amorphous TiO_2 transform into its crystalline form without the need for any additional heat treatment step which is required in other electrochemical methods. There are a few researches reporting the growth of photocatalyst layers by MAO method. He et al. prepared TiO_2–WO_3 photo-catalysts layers incorporated with fluorine ions [22]. Bayati et al. synthesized nano-structured TiO_2–WO_3 and TiO_2–V_2O_5 composite and pure TiO_2 layers by MAO process and studied effect of electrical parameters on their photocatalytic performance [23-25]. Very recently, Stojadinovic et al. produced Al_2O_3–ZnO, TiO_2–WO_3 and TiO_2:Eu^{3+} photocatalyst layers and probed their photocatalytic properties with increasing MAO time [26-28].

In our previous study, we characterized surface morphology and evaluated the long-term corrosion behavior of the Zr-containing layers fabricated on titanium by micro arc oxidation method [29]. In the present work, the dependence of the catalytic performance of the TiO_2-ZrO_2 composite layers on duty cycle and additive concentration are discussed in detail in order to provide vital information for synthesizing efficient photocatalytic composite layers in degradation of hazardous aqueous compounds.

2. Experimental procedure

2.1. Sample preparation

The disk specimens of commercially pure titanium (CP-grade 2) with working area of $\sim$ 7 cm^2 were cut from a sheet with 0.8 mm thickness. For metallographic characterization, the specimens were grounded to a 1200 grit SiC finish, using water as a lubricant, degreased in ethanol, and dried in warm air. The specimens connected to the positive pole of the power supply were encircled by a hollow coil pipe made of ASTM 316 stainless steel through which cold water was run for cooling the solution. The electrolyte itself was agitated by a mechanical stirrer. The specimens then MAO-treated for 7 min in an electrolytic solution containing sodium dihydrogen phosphate (NaH_2PO_4) in 1 L of distilled water as the base electrolyte and sodium zirconate (Na_2ZrO_3) and sodium silicate (Na_2SiO_3) as additives. The composition of the electrolyte systems with their respective conductivity and pH values can be found in Table 1. The conductivity of the electrolytes was measured by MC226 basic conductivity meter (Mettler-Toledo). The micro arc oxidation process was carried out using a pulsed DC electrical power source at a fixed voltage of 500 V. The MAO process was conducted at three duty cycles viz. 30%, 50% and 70%, with a fixed frequency of 1000 Hz. The pure titania and composite layers were named TC-D and TZC-D, respectively; where C is the electrolyte code and D is the duty cycle of process.

5

2.2. Characterization of MAO layer

The field emission scanning electron microscopy (ZIESS ΣIGMA VP) with an accelerating voltage of 15.0 kV was used to study the morphology of the layers. The FE-SEM was coupled with energy dispersive spectroscopy (EDS) to assess elemental composition of the synthesized layers. The phase composition of layers was identified using a Philips X'Pert-Pro X-ray diffractometer with Cu Kα radiation (λ=1.54060Å). The behavior of different TiO_2-ZrO_2 layers was also studied by Electrochemical impedance spectroscopy (EIS). The EIS measurements were conducted using a Solartron 1260 model frequency response analyzer with an AC amplitude of 10 mV around OCP over the frequency range of $0.1–10^5$ Hz. The collection and evaluation of EIS data and curve fitting via circuit modeling were implemented using ZView® software. Photoluminescence (PL) spectra was measured on a Horiba Jobin-Yvon spectrophotometer under the excitation of 325 nm emission line from a Cd-He laser.

2.3. photocatalytic experiments

The photocatalytic activity of the prepared composite layers was evaluated by photocatalytic degradation of aqueous methylene blue (MB) solution under UV irradiation. Samples of 2 cm × 1 cm, as catalysts, were immersed into 50 ml aqueous methylene blue solution (10mg/l) in the cylindrical quartz cell with the size of 30 mm in diameter and 100 mm in height. The UV light was irradiated from a 30 W UV lamp with a maximum UV irradiation peak of 365 nm perpendicular to the surface of the layer through the sidewall of quartz cell. The distance between the layer and the lamp was 7 cm. The light intensity was measured as 1.6 mW cm^{-2} using a radiometer (UV(A)-254, Lutron Electronic) attached to the outer wall of the quartz cell. Prior to irradiation, the solution and the samples were left in dark for 30 min to ensure establishment of the adsorption/desorption equilibrium. During the UV irradiation, a fixed quantity of the solution was taken out at certain time intervals to measure the absorption and the concentration. The absorptivity measurements were conducted by recording UV-vis spectra of MB using a PerkinElmer UV-vis spectrophotometer.

6

Results and discussion

3.1. Morphology, chemical and phase composition of MAO layers

Fig. 1 displays the SEM micrographs of the surface morphology of the layers produced at different duty cycles in electrolytes with various additive concentration. All the layers show porous microstructure with crater-like pores representing a typical characteristic of MAO layers. The average pore size of the layers increases with duty cycle at a constant concentration of sodium zirconate. While we can identify pores with sizes of $< 0.5\ \mu m$ in all the layers, the largest pore size increases from $\sim 3.6\ \mu m$ to $\sim 7.4\ \mu m$ in diameter as the duty cycle increases from 30% to 70%. For the layers prepared at D=30% and 70%, nearly 80% of the pores have a size less than $0.5\ \mu m$, which are actually independent of duty cycle. It can be concluded that the main effect of duty cycle on layer morphology is involved in enlarging of small-number pores. At duty cycle of 30%, the 2 g/l additive leads to an increase in layer porosity, but when the additive concentration increases to 4 g/l the layer surface becomes much more uniform with much less number of small-size pores (region "a"). By duty cycle of 70%, the pore size increases significantly with additive concentration. In fact, increasing additive concentration causes a change from a dense population of pores to smaller population of large-size pores uniformly distributed on the surface of the layers. The increasing trend of pore size with increasing additive concentration can be attributed to the decrease of electrolyte electrical resistivity when utilizing higher concentrated electrolytes. With decreased electrolyte resistivity, more energetic electric avalanches occur, which results in intensified microdischarges taking place in the vicinity of the anode. Such strong electric sparks lead to an increase in size of discharge channels, i.e. layer porosity.

When the duty cycle is further increased, the layer shows larger pores corresponding to increased microdischarge intensity, although fine pores are still present. The layer prepared at duty cycle of 70% in electrolyte containing 4g/l additive displays a partly-established "coral reef" structure, which is characterized by many large, scattered protuberances (region "b") on the layer surface along with large residual discharge channels (region "c") which are known to be caused by gas envelope and oxide layer breakdown, respectively [30].

According to the EDX spectra measured at three distinct locations in our previous study [29], the discharge channels emanating from microdischarges of strong dielectric breakdown, could provide paths for substrate elements to attach into the layer. The so called type-B microdischarges would be more intense than any other kind of microdischarges at the electrolyte/layer interface or at the middle of the layer capable of drawing elements from substrate into the layer. On the other hand, less intense microdischarges tracing from small-size pores, known as type-C, which are dominant at lower duty cycles incorporate elements derived from electrolyte into the layer; however, the near surface type-A microdischarges originating from gas envelope breakdown at high duty cycle are the main force responsible for pulling electrolyte species such as zirconium onto the layer, leaving traces of sintered protrusions on the layer.

When using lower concentrated electrolyte, less intense microdischarges produced at lower duty cycles promote zirconium employment from electrolyte into the layer, whereas the intensified microdischarges at higher duty cycles rather dispel the electrolyte anions from layer surface. Contrary to the previous working electrolyte, utilizing higher additive concentration changes the sparking regime at higher duty cycle and Zr-containing species can be adsorbed on the surface of the layer by near surface microdischarges. Based on element composition of the MAO layers obtained by EDS analysis (see Table 2), for the layers fabricated in A4 electrolyte maximum concentration of Zr and P is obtained at high duty cycle, conversely to the case of layers formed in A2 electrolyte reaching that at low duty cycle. The

8

cause of such different behavior when applying higher concentrated electrolyte is the microdischarges of gas envelope breakdown that can sinter more elements from applied electrolyte into the layer. In fact, with increased duty cycle, microdischarges arising from breakdown of gas envelope enhance the sintered function of discharges, and as a result, the prepared layer would contain more elements from the electrolyte.

XRD patterns of the pure TiO_2 and composite MAO layers formed at various duty cycles and electrolytes are shown in Fig. 2. It is determining for photocatalytic performance to take the variation of anatase and rutile phase peak intensities into account, regarding higher photoactivity of anatase phase relative to rutile phase in the layers. It can be observed that the peak intensity of titanium dioxide in the form of anatase in composite layers increases with duty cycle, indicating the increased layer thickness, meanwhile, the increase of rutile phase intensity with duty cycle in the layers formed at A2 electrolyte is more pronounced than that in layers formed at A4 electrolytes. it appears that for the layers formed at A4 electrolyte the phase transformation in TiO_2 from anatase to rutile phase is blocked to some extent as the duty cycle increases, which is attributed to the increased incorporation of zirconium and silicon oxides at higher duty cycles contributing to thermal stability enhancement of titania against phase transformation. In contrast, for the layers formed at A2 electrolyte, the intensity of rutile phase appears to increase more noticeably as the incorporation of electrolyte species drops with increasing duty cycle leading to a poorly blockage of anatase to rutile transformation. The transformation is likely to occur when either the concentration of electrolyte or duty cycle of process increase. The increased electrolyte concentration leads to a decline in electrochemical resistance of electrolyte followed by higher current passing through the cell generating more intensified microdischarges, which in turn facilitate titania phase transformation. In the case of increased duty cycle, longer on-times result in longer lasting microdischarges either on the surface or deep inside the layers and formation of higher XRD peak intensities. Near surface microdischarges evolved at higher concentrated electrolytes draw more

9

elements from electrolyte, which hinder TiO_2 phase transformation, whereas deep microdischarges rather give rise to TiO_2 phase transformation due to deficient element employment from electrolyte so as to properly block the phase transformation. This different behavior points out that the influence of duty cycle on titania phase transformation depends on the microdischarge regime. The formation of the Ti–O–Zr bonding structure was confirmed by relatively weak characteristic diffraction peaks related to $ZrTiO_4$ oxide according to XRD spectra of the TiO_2-ZrO_2 composite layers. Similar ionic radius of Ti^{4+} (0.068 nm) and Zr^{4+} (0.072 nm) allows Zr^{4+} to substitute Ti^{4+} in the crystal lattice of TiO_2 through interaction between TiO_2 and ZrO_2. The crystalline TiO_2, ZrO_2 and $ZrTiO_4$ were included in the layer prepared in the mixture electrolyte of phosphate and zirconate. The formation mechanism of titania-zirconia layers by MAO process could be as follows:

Decomposition of water as cathodic process and oxidation of hydroxyl groups and water molecules as anodic process are responsible for oxygen generation on anode surface. Meanwhile ionization of sodium hydrogen phosphate occurs resulting in generation of further OH^- anions. The chemical equations related to the electrochemical reactions are given below:

$$NaH_2PO_4 \rightarrow Na^+ + H_2PO_4^- \tag{1}$$

$$H_2PO_4^- + H_2O \rightarrow H_3PO_4 + OH^- \tag{2}$$
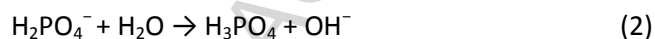
OH^- from hydrolysis of water accelerates ionization of sodium zirconate, as shown in reaction (4), leading to deposition of $ZrO(OH)_2$. Decomposition and hydrolysis of sodium zirconate takes place according to the following reactions:

$$Na_2ZrO_3 \rightarrow Na_2O + ZrO_2 \tag{3}$$

$$Na_2ZrO_3 + 2H_2O \rightarrow ZrO(OH)_2 + 2NaOH \tag{4}$$

10
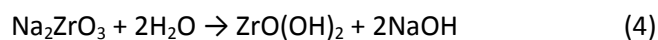
Zirconium hydroxide ($ZrO_2 \cdot nH_2O$) is colloidal particle and since its point of zero charge is at pH=6.8, $ZrO(OH)_2$ should be electronegative in alkaline electrolyte [31]. Therefore, $ZrO(OH)_2$ and OH^- anions migrate toward the anode surface due to the electrical field between anode and cathode. In fact, the zeta potential of the colloidal $ZrO(OH)_2$ decreases as the pH of the electrolyte increases with increasing electrolyte concentration. This high negative potential could enhance the attraction of particles toward the anode substrate. The higher the alkali content, the stronger the attractive forces between the anode and negatively charged $ZrO(OH)_2$. As a result, more particle will be drawn toward the anode surface when operating A4 solution, which shows the highest pH as is seen in Table 1. Eventually, $ZrO(OH)_2$ generates ZrO_2 under high temperature and pressure in the vicinity of anode surface. It is anticipated that the molten system dissolves the ZrO_2 and other anions. Therefore, the incorporation of particles could be accomplished by the combined processes of electrophoretic forces and the physical mixing through perturbation caused by electric discharges. The reaction between Ti^{4+} from anodic dissolution of titanium substrate and O^{2-} from water electrolysis and OH^- at the metal/oxide and oxide/electrolyte interfaces takes place according to:

$$ZrO(OH)_2 \rightarrow ZrO_2 + H_2O \qquad (5)$$

$$Ti^{4+} + 2O^{2-} \rightarrow TiO_2 \qquad (6)$$

$$Ti^{4+} + 4(OH)^- \rightarrow Ti(OH)_4 \rightarrow TiO_2 + 2H_2O \qquad (7)$$

11

The incorporation of ZrO_2 from electrolyte into titania during MAO process to form hybridized TiO_2-ZrO_2 layer demonstrates the participation of Zr^{4+} in Ti–O– bonds. Consequently, the doping of TiO_2 lattice with Zr atoms enhances the photocatalytic activity by formation of complex defects comprising Zr atoms and oxygen vacancy according to the chemical reaction in Kröger and Vink notation:

$$ZrO_2 \rightarrow Zr_{Ti'} + V_{\ddot{O}} + O_o + 1/2O_2 + 2e^- \qquad (8)$$
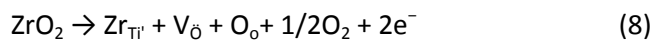
where $Zr_{Ti'}$ is the Zr ion at a Ti lattice site with a single charge deficiency, $V_{\ddot{O}}$ is a doubly ionized oxygen vacancy, O_o is an oxygen ion in the normal lattice site where the concentration of the intrinsic defect ($V_{\ddot{O}}$) becomes equal to the concentration of the extrinsic impurity [13]. The life-prolonged photo generated electron and hole pairs trapped by oxygen vacancies and Zr^{4+} surface states act as redox centers capable of degrading and mineralizing reactive toxic dyes into inorganic molecules.

3.2. UV- visible absorption spectra

Ultraviolet–visible diffuse reflectance spectroscopy (UV–vis/DRS) is used to investigate the optical performance of the pure TiO_2 and TiO_2-ZrO_2 composite layers prepared in electrolytes containing different additive concentrations. In crystalline semiconductors, the inter-band absorption is related to incident photon energy and band gap energy E_g according to the equation:

$$\alpha(v)hv = B(hv - E_g)^m \qquad (9)$$

Where E_g is optical band gap energy, B is proportionality constant, hv is incident photon energy and m is an index determined by the type of electronic transition responsible for the optical absorption and obtains values of 1/2 and 2 for the allowed direct and indirect transitions, respectively. We can derive absorption coefficient as a function of wavelength by rewriting Eq. (9):

$$\alpha(\lambda) = B(hc)^{m-1}\lambda(\frac{1}{\lambda} - \frac{1}{\lambda_g})^m \qquad (10)$$

Where λ_g, h and c are wavelength corresponding to the optical gap, Plank's constant and the velocity of the light, respectively. The absorption coefficient α is directly proportional to the film absorbance measured from the spectrometer according to Beer-Lambert's law: $\alpha = \frac{2.303\,Abs}{d}$, where d and Abs are the film thickness and film absorbance respectively, so it is possible to introduce the absorption spectrum fitting (ASF) by rewriting Eq. (10):

$$Abs(\lambda) = B_1\lambda(\frac{1}{\lambda} - \frac{1}{\lambda_g})^m + B_2 \qquad\qquad (11)$$

Where $B_1 = \left[B(hc)^{m-1} \times \frac{d}{2.303}\right]$ and B_2 is a constant which takes into account the reflection. Using Eq. 11, it is possible to calculate optical band gap by absorbance spectrum fitting method without any need to the film thickness. Thus we can derive the value of band gap, in eV, from the parameter λ_g using $E_{gap}^{ASF} = 1239.83/\lambda_g$. The coordinates of (Absorbance vs. wavelength) was established to construct the plots to estimate λ_g values by extrapolating the linear region of $(Abs/\lambda)^{1/m}$ vs. $(1/\lambda)$ curve at $(Abs/\lambda)^{1/m} = 0$. The UV–vis DRS spectra of the pure TiO_2 layer and the TiO_2–ZrO_2 composite layers prepared at various duty cycles are shown in Fig. 3a. It is apparently observed that the absorption edge of the layers shifted toward longer wavelengths with increasing additive concentration. The enhanced absorption in the longer wavelength region may be associated with the introduction of a dopant energy level into the band gap of TiO_2, generating electron capture centers acting as shallow acceptors which contribute to the separation of electrons and holes. The red shifted absorption edge results from the electronic transitions between the dopant level, valence and conduction band of Zr-doped TiO_2 layer [32, 33]. It is expected that the optical band gap for the pure TiO_2 layer changed by incorporation of ZrO_2. in the case of the layers prepared at A4 electrolyte, the absorption edge shifts towards shorter wavelengths and then goes back towards longer wavelength with increasing duty cycle. The shifting of the absorption edge could be explained by two competing outcomes resulting from zirconium ions incorporated into the layer, the extent of which determines the red shift or blue shift of absorption

13

edge. As is seen from EDS results (Table 2), when the duty cycle of process is increased to 50%, a very small amount of zirconium and silicon ions is further added to the layer, so that the contribution of zirconium ions to red shift of absorption edge may be negligible; however, the blockage effect on anatase to rutile phase transformation becomes more prevalent leading to blue shift of adsorption edge. The band gap of the layer increases as the ratio of anatase to rutile phase increases, having in mind that the anatase has a wider band gap compared to rutile. As the duty cycle increases to 70%, a tremendous increase in the Zr incorporation makes the red shift of absorption edge more prevalent. For evaluation of the band gap values, $(A/\lambda)^{1/m}$ versus $(1/\lambda)$ was plotted, as shown in Fig. 3b with the inset presenting the obtained band gap values. The value of m for TiO_2 and ZrO_2 is 2, as they are indirect band gap semiconductors. It is evident that the band gap energy values of the composite layers decreased from that of the pure titania layer, indicating that the composite layers might have superior photocatalytic activity. It has been reported that doping metal ions into the TiO_2 lattice causes the band gap energy to decrease by insertion of continuous energy levels between the valence band maximum (VBM) and conduction band minimum (CBM) [13]. In addition, utilizing electrolytes with higher concentration heats the anode up more due to stronger microdischarges rising from higher electrolyte conductivity. As a result, transformation of meta-stable anatase phase to the thermodynamically stable rutile phase with smaller band gap than the anatase may occur at higher temperatures leading to decreased band gap of the composite layer.

3.3. Photoluminescence (PL) spectra

To study the fate of the photo-generated carriers, as well as transfer or separation of electron hole pairs, we measured photoluminescence spectra of the pure TiO_2 layer and layers formed at A2 and A4 electrolyte, as shown in Fig. 4. The composite layers have lower PL intensity than the Pure TiO_2 layer; meanwhile, the PL intensity of composite layers decreases with additive concentration. PL emission spectra of the layers features a major emission peak at the range of 350 to 390 nm equal to the TiO_2

band gap energy in the UV region which is attributed to the radiative recombination of photo-generated charge carriers. Moreover, the broad excitonic PL band in the visible region between 450 and 570 nm is assigned to the emission of photo-generated carriers from energy levels corresponding to oxygen vacancies, oxide related surface defects and impurities. As the photoluminescence spectra is the result of recombination of generated electrons and holes, a lowering of overall PL intensity corresponds to the decrease in recombination rate and hence increase of photocatalytic activity of the layers. In fact, the reduction in the PL intensity could be attributed to the trapping of charge carriers by oxygen vacancies and Zr^{4+} surface states, which facilitates the charge separation process and charge transfer to the surface by reducing mean free path of charge carriers [34, 35]. We note that the layer prepared at A4 electrolyte and highest duty cycle reveals the lowest PL intensity, pointing that this layer should have a superior separation and longer lifetime of electrons and holes. The weak shoulder emission peak at 480 nm is attributed to the indirect recombination via trap levels formed by oxygen impurities as a kind of defects in TiO_2-ZrO_2 layers.

3.4. EIS measurements

The electrochemical responses of the photocatalysts are studied by analyzing the EIS spectra at the open circuit potential in the dark. The charge transfer and recombination behavior of the layers were assessed by comparing the interfacial resistance and capacitance values of the developed MAO layers at different duty cycles and electrolyte concentrations. Complex and Bode plots obtained from layers produced in electrolyte A2 and A4 are presented in Fig. 5a-d. The Bode plots are split into two sections, i.e. time constants characterizing outer porous region and inner compact region of the layer. The Nyquist spectra of layers exhibits a semicircle at high frequency attributed to charge-transfer process occurring at photocatalyst/electrolyte interface as a minor feature of the electrical double layer, which are generated typically on systems with high surface area like a porous surface. The linear behavior at lower frequencies (45° segment) discernible for the layers formed in electrolyte A4 represents the ionic

diffusion process. Higher incorporation of ZrO_2 into the layers prepared in electrolyte A4, would generate a great amount of separated electrons and form a double layer on their surface which appears as an almost-straight part of the diffusion portion of Nyquist plots. The phase angle of about $\sim \pi/8$ in the middle frequency region of Bode plots is an evidence for controlled impedance behavior [36]. From Bode plots of the composite layers, it seems that the breakpoint frequency f_b (frequency of $45^{°}$ phase angle) shifted toward higher frequencies with increased duty cycle signifying increased exposed surface area provided for charge carriers. This benefits photocatalysis by providing full contact with O_2 during the reaction process and higher accessibility of photocatalyst surface by electrolyte ions. Notice that the extent of exposed surface area provided by layers varies with the duty cycles corresponding with variation of layer porosity.

The EIS experimental data were fitted to a suggested equivalent circuit with a modification to take into account the non-ideal behavior of the capacitive elements due to different physical phenomena such as surface heterogeneity (Fig. 6a). This circuit is based on the model applied for porous TiO_2 [37, 38] containing two time constants in order to properly address the high and low frequency features of the layer/electrolyte interface, impedance response of the pores and the process occurring at the electrode surface. In this circuit the paralleled elements of CPE_i and R_i are associated with the low frequency response of the oxide layer electrical components, namely to the surface adsorbed ionic species pseudocapacitance C_i and resistance R_i of the layer. The electrolyte resistance (R_s) is in series with a parallel combination of charge transfer resistance (R_{ct}) and constant phase element (CPE_o) ascribed to the charge transfer kinetics across the interface of porous layer and electrolyte, namely to the response of double layer capacitance characterized by CPE_o, and charge transfer resistance characterized by R_{ct} [39, 40]. So, the constant phase elements are referred to electrical double layer capacitance at layer/electrolyte interface and pseudocapacitance of the layer. To account for the non-ideality of the system (distributed surface reactivity, surface inhomogeneity, roughness or electrode porosity [41])

16

pure capacitances (C) of the layer components were replaced with constant phase element (CPE). The impedance of constant phase element (Z) is expressed by the following equation [42]:

$$Z = \frac{1}{Q(j\omega)^n} \qquad (12)$$

Where Q ($\Omega^{-1}\,s^n\,cm^{-2}$) is the admittance of CPE, ω (rad/s) the angular frequency and n as the deviation parameter which has been believed by researchers to be inversely proportional to the surface roughness [43]. For the diffusion behavior of the layers prepared in electrolyte A4, another equivalent circuit model, which contained semi-infinite Warburg impedance (Z_W), was proposed (Fig. 6b) to account for the ion transport through the layer. The Warburg impedance is represented as $Z_W = A/(j\omega)^m$, where A and m are the Warburg element constant and exponent, respectively. Table 3 summarizes the fitting results of the different EIS parameters obtained from the impedance measurements of the layers fabricated in different electrolytes.

The electrochemical double layer capacitance (C_{dl}) is correlated with CPE through the following equation by Hsu and Mansfeld [44]:

$$C_{dl} = \frac{Q(\omega_{max})^{n-1}}{\sin(n(\pi/2))} \qquad (13)$$

Where ω_{max} is the frequency at which the imaginary part of impedance ($-Z_i$) reaches its maximum value [45]. Thus, Q value which reflects the dielectric behavior of the layer/electrolyte interface, becomes C for $n = 1$. The effective capacitance (C_{eff}) without the derivation by Hsu and Mansfeld [44] in terms of ω_{max} associated with CPE parameters can be expressed as:

$$C_{eff} = Q^{1/n}R_{CPE}^{(1-n)/n} \qquad (14)$$

Where R_{CPE} is the resistance of the layer in parallel with CPE [46]. From the data of Table 3, the average double layer capacitance, C_{dl}, and oxide layer capacitance, C_i, were calculated using the above equation (see Table 4).

Based on the transmission line model explained by Wang et al. [47], charge recombination resistance is corresponding to the charge transfer at the layer/electrolyte interface. A lower charge transfer resistance is indicative of recombination suppression by improved charge transport to the electrolyte. The improvement of charge transport kinetics seen in layers containing higher amount of zirconium additive is attributed to the formation of higher surface trap states which act as mediators for charge transfer to electrolyte. Moreover, the drop in the impedance values is corresponding with the generation of great amount of electrons on their surface.

The high frequency semicircle in the EIS spectra of the layers prepared in electrolyte with constant additive concentration varies in diameter with duty cycle. Moreover, it appears that the variation trend of the EIS response and semicircle diameter of the coated samples with duty cycle of the process changes with additive concentration of the working electrolyte. In particular, among the layers prepared in electrolyte A2, the layer obtained at D=30%, namely TZA2-30, shows smaller semicircle and impedance values, of which the amount of Zr incorporated was higher. Lower charge transfer resistance implies higher electron transfer rate and charge recombination suppression in TiO$_2$. Presumably, the performance of the layer photocatalysts tends to decrease with increasing duty cycle when utilizing lower concentrated electrolyte. With increasing additive concentration, low interfacial charge transfer discernible from smaller semicircle is observed for the specimen MAO treated at high duty cycle, namely TZA4-70, suggesting better photocatalytic activity among the layers fabricated in electrolyte A4. The reason is the processing condition at which the microdischarge regime incorporates additive species into the layer much easier and forms a surface layer with higher porosity, which can enhance photocatalytic performance. In sum, a certain duty cycle during fabrication process favors charge transfer at the

layer/solution interface and suppresses charge recombination through increased ZrO_2 incorporation into the TiO_2 layer and higher accessibility of active surface to electrolyte solution ions.

The solution resistance R_s at layer/electrolyte interface reflects electronic and ionic transport properties of the interface corresponding with intrinsic resistance of electrode and bulk electrolyte respectively. Comparing lower value of R_s for TiO_2-ZrO_2 composite layers (below 6 Ωcm^2) with that of pure TiO_2 layer (17 Ωcm^2) reveals that conductivity of layers coupled with ZrO_2 was enhanced greatly. The charge transfer kinetic and physical absorption of electrolyte ions on the layer surface is interpreted through the values of double layer capacitance represented by values of (C_{dl}). Among the layers prepared in electrolyte A4, TZA4-70 exhibits the highest C_{dl} which is indicative of providing more accessible sites to the mobile charges near surface of this layer. The double layer capacitance value (C_{dl}) correlates similarly to the capacitance of the oxide layer (C_i); higher capacitance of the photocatalyst leads to higher capacitance of the double layer. It has been reported that an increase in the oxide layer capacitance value may lead to higher charge densities at the layer-solution interface and therefore to an increase in the capacitance of the double layer and a lower resistance [38].

The CPE exponents (n) of electrical double layer were <1, which provided a strong verification of the heterogeneity of photocatalyst surface. The values of n in constant phase element of electrical double layer decreased with increasing duty cycle indicating an increase in surface roughness, which was consistent with the SEM results in Fig. 1.

3.5. Photocatalytic activity

Photocatalytic decolorization of methylene blue solution was carried out by various photocatalyst layers in order to evaluate their photocatalytic efficiency. Fig. 7 illustrates photocatalytic activity of different layers for degradation of MB from aqueous solution as a function of time under UV light irradiation. The activity of pure TiO_2 layer was lower than those of composite layers, signifying that the presence of ZrO_2

in TiO$_2$ increases the photocatalytic performance of the composite layers. The crucial factors that influence the activity of photocatalysts in degradation of organic pollutants include the light absorption, charge transportation and separation [38, 48]. It was proposed that the substitution of Ti lattice ions with Zr ions leads to formation of Ti-O-Zr bond due to high energy plasma-chemical interaction between TiO$_2$ and ZrO$_2$. The conduction band (CB) and valence band (VB) of TiO$_2$ and ZrO$_2$ align well with each other which help prolong the separation time of electron-hole pairs. Moreover, electrons and holes recombination may be prevented by transferring photo-generated electrons from conduction band of ZrO$_2$ to lower-lying conduction band of TiO$_2$. Therefore, the enhancement of charge separation by trapping holes and generation of OH radicals acting as powerful oxidants may improve photo degradation of dye molecules [49]. As a result of electron transfer from CB of ZrO$_2$ to CB of TiO$_2$, strong oxidizing centers on ZrO$_2$ surface states lead to trapping of positive holes in the VB of ZrO$_2$. The electron centers formed in the CB of TiO$_2$ combine with O$_2$ molecules to form O$_2\bullet^-$ free radicals and holes in VB of ZrO$_2$ combine with OH$^-$ and H$_2$O, thereby generating $\bullet$OH free radicals. The degradation of MB occurs via redox reactions of the produced free radicals with highly active species [13, 50].

It has been proved that the photocatalytic degradation of MB obeys the pseudo-first order kinetics [51]. Therefore, assessment of the photocatalytic activities of the layers prepared by MAO method could be implemented appropriately by determination of rate constant. The degradation behavior of the layers seemed to follow the pseudo-first order model; hence the reaction rate constants were calculated by the equation: $ln(C_0/C) = -kt$. Fig. 8 depicts the linear variation of the logarithms of relative concentration of MB solution $ln\,(C_0/C)$ as a function of the irradiation time for TiO$_2$-ZrO$_2$ layers prepared in different electrolytes and duty cycles. The apparent reaction rate constants of the photocatalytic degradation of MB are listed in Table 5.

20

The photocatalytic performance of the layers reaches its maximum value at a certain duty cycle varying with the additive concentration. The reason lies within the fact that the content of the ZrO_2 incorporated into the layer, affecting the photo-activity, changes with duty cycle and electrolyte additive concentration as a result of related microdischarge regime. Although the exposed surface of the composite layers increases with duty cycle, corresponding with the porosity, photocatalytic activity of the layers depends directly on the zirconia incorporation into the layer. The presence of ZrO_2 improves the photochemical properties of the layers by reducing the recombination of photo-generated electrons and holes. The higher the zirconia content in the layer the better the photocatalytic performance; as a result, the photocatalytic activity of composite layers produced in electrolyte A2 weakens with duty cycle, as less Zr is incorporated into the layer at high duty cycle. Decreased photocatalytic activity of the layers formed in A2 electrolyte with duty cycle could also be ascribed to the diminished active centers and/or inferior surface morphology. SEM micrographs (Fig. 1) reveal that the layers obtained in highest duty cycle at A2 and A4 processing electrolytes feature different morphology in terms of pore structure. At A2 electrolyte the TZA2-70 layer reveal a crater-like structure with a flattened surface containing less number of discharge channels, whereas the TZA4-70 layer is characterized by zirconium enriched surface protuberances with a large number of tiny pores. Such morphology change, caused primarily by microdischarge regime, influences the overall photocatalytic activity of the layers, by interfering the transport of reactants (light as immaterial reactant and/or dye) through altering surface area of the layer or simply the number of active sites. However, among the composite layers the photocatalytic activity of the TiO_2-ZrO_2 composite layer fabricated in electrolyte A4 at duty cycle of 70% is the most outstanding; therefore, these parameters were considered the most appropriate synthesis conditions to produce TiO_2-ZrO_2 composite layers via MAO method. The enhancement of the photocatalytic activity could be mainly attributed to the reduction in electron–hole pair recombination in TiO_2 with the introduction of ZrO_2 due to the stepwise energy level in the composites, which have been confirmed by

21

the UV–vis absorption, photoluminescence spectra and EIS measurements. Therefore, it is evident that microdischarge regimes determine the amount of zirconia incorporation to form ZrO_2–TiO_2 composites and controls the photochemical performances of the layers. This signifies that the photocatalytic activity of composite depends upon microstructural characteristics and layer porosity, however; optimum conditions must be attained to produce layers with improved activity.

Conclusion

In the present study, using micro arc oxidation, TiO_2-ZrO_2 composite layers were prepared at different duty cycles and electrolytes with varying additive concentration. The effect of duty cycle and additive concentration on the surface morphology and photocatalytic activity of the layers were studied. It was found that the pore size increases with increasing additive concentration and duty cycle. It was also observed that the absorption edge of the layers shifted toward longer wavelengths when the additive concentration increased. Accordingly, the band gap energy values of the composite layers were lower as compared with that of the pure TiO_2 layer. The highest MB degradation was obtained with the TiO_2-ZrO_2 composite layer produced in electrolyte A4 under duty cycle of 70% when operating under UV. The enhanced photocatalytic activity may be attributed to the interaction between TiO_2 and ZrO_2 which allowed for effectively reduction of photo-generated electrons-hole pairs recombination.

The combination of microstructural characterization with optical measurements and EIS data was proven to be an efficient tool for understanding the electronic properties of the composite layers. The EIS date are of vital importance in better interpreting the difference between the interfacial characteristics of photocatalyst layers.

References

[1] M. Miyauchi, A. Nakajima, T. Watanabe, K. Hashimoto, Photocatalysis and Photoinduced Hydrophilicity of Various Metal Oxide Thin Films, Chem. Mater., 14 (2002) 2812-2816.

[2] S. Šegota, L. Ćurković, D. Ljubas, V. Svetličić, I.F. Houra, N. Tomašić, Synthesis, characterization and photocatalytic properties of sol–gel TiO2 films, Ceram. Int., 37 (2011) 1153-1160.

[3] Z. Ambrus, K. Mogyorósi, Á. Szalai, T. Alapi, K. Demeter, A. Dombi, P. Sipos, Low temperature synthesis, characterization and substrate-dependent photocatalytic activity of nanocrystalline TiO2 with tailor-made rutile to anatase ratio, Applied Catalysis A: General, 340 (2008) 153-161.

[4] J. Li, X. Yang, X. Yu, L. Xu, W. Kang, W. Yan, H. Gao, Z. Liu, Y. Guo, Rare earth oxide-doped titania nanocomposites with enhanced photocatalytic activity towards the degradation of partially hydrolysis polyacrylamide, Appl. Surf. Sci., 255 (2009) 3731-3738.

[5] Y.-H. Xu, C. Chen, X.-L. Yang, X. Li, B.-F. Wang, Preparation, characterization and photocatalytic activity of the neodymium-doped TiO2 nanotubes, Appl. Surf. Sci., 255 (2009) 8624-8628.

[6] J.A. Rengifo-Herrera, C. Pulgarin, Photocatalytic activity of N, S co-doped and N-doped commercial anatase TiO2 powders towards phenol oxidation and E. coli inactivation under simulated solar light irradiation, Solar Energy, 84 (2010) 37-43.

[7] J. Wang, Y. Lv, Z. Zhang, Y. Deng, L. Zhang, B. Liu, R. Xu, X. Zhang, Sonocatalytic degradation of azo fuchsine in the presence of the Co-doped and Cr-doped mixed crystal TiO2 powders and comparison of their sonocatalytic activities, J. Hazard. Mater., 170 (2009) 398-404.

[8] Y. Liu, J. Liu, Y. Lin, Y. Zhang, Y. Wei, Simple fabrication and photocatalytic activity of S-doped TiO2 under low power LED visible light irradiation, Ceram. Int., 35 (2009) 3061-3065.

[9] X.-F. Wu, H.-Y. Song, J.-M. Yoon, Y.-T. Yu, Y.-F. Chen, Synthesis of Core–Shell Au@TiO2 Nanoparticles with Truncated Wedge-Shaped Morphology and Their Photocatalytic Properties, Langmuir, 25 (2009) 6438-6447.

[10] H. Tada, K. Teranishi, S. Ito, H. Kobayashi, S. Kitagawa, H2 Generation by Cycling Dark Adsorption and Successive Photoinduced Desorption of 2-Mercaptopyridine on/from Ag-Core/Pt-Shell Nanoparticles Loaded on TiO2, Langmuir, 16 (2000) 6077-6080.

[11] C.-C. Ou, C.-S. Yang, S.-H. Lin, Selective photo-degradation of Rhodamine B over zirconia incorporated titania nanoparticles: a quantitative approach, Catalysis Science & Technology, 1 (2011) 295-307.

[12] Y. Chi, Q. Yuan, Y. Li, L. Zhao, N. Li, X. Li, W. Yan, Magnetically separable Fe3O4@SiO2@TiO2-Ag microspheres with well-designed nanostructure and enhanced photocatalytic activity, J. Hazard. Mater., 262 (2013) 404-411.

[13] B.M. Pirzada, N.A. Mir, N. Qutub, O. Mehraj, S. Sabir, M. Muneer, Synthesis, characterization and optimization of photocatalytic activity of TiO2/ZrO2 nanocomposite heterostructures, Materials Science and Engineering: B, 193 (2015) 137-145.

[14] A.K. Singh, U.T. Nakate, Microwave synthesis, characterization, and photoluminescence properties of nanocrystalline zirconia, TheScientificWorldJournal, 2014 (2014) 349457.

[15] I.C. Cosentino, E.N.S. Muccillo, R. Muccillo, Development of zirconia-titania porous ceramics for humidity sensors, Sensors and Actuators B: Chemical, 96 (2003) 677-683.

[16] Q. Yuan, Y. Liu, L.-L. Li, Z.-X. Li, C.-J. Fang, W.-T. Duan, X.-G. Li, C.-H. Yan, Highly ordered mesoporous titania–zirconia photocatalyst for applications in degradation of rhodamine-B and hydrogen evolution, Microporous Mesoporous Mater., 124 (2009) 169-178.

[17] M.E. Zorn, D.T. Tompkins, W.A. Zeltner, M.A. Anderson, Photocatalytic oxidation of acetone vapor on TiO2/ZrO2 thin films, Applied Catalysis B: Environmental, 23 (1999) 1-8.

24

[18] J.H. Schattka, D.G. Shchukin, J. Jia, M. Antonietti, R.A. Caruso, Photocatalytic Activities of Porous Titania and Titania/Zirconia Structures Formed by Using a Polymer Gel Templating Technique, Chem. Mater., 14 (2002) 5103-5108.

[19] A. Kambur, G.S. Pozan, I. Boz, Preparation, characterization and photocatalytic activity of TiO2–ZrO2 binary oxide nanoparticles, Applied Catalysis B: Environmental, 115–116 (2012) 149-158.

[20] J. Zhang, L. Li, D. Liu, J. Zhang, Y. Hao, W. Zhang, Multi-layer and open three-dimensionally ordered macroporous TiO2–ZrO2 composite: diversified design and the comparison of multiple mode photocatalytic performance, Mater. Des., 86 (2015) 818-828.

[21] R.A. Lucky, Y. Medina-Gonzalez, P.A. Charpentier, Zr doping on one-dimensional titania nanomaterials synthesized in supercritical carbon dioxide, Langmuir, 26 (2010) 19014-19021.

[22] J. He, Q.Z. Cai, Y.G. Ji, H.H. Luo, D.J. Li, B. Yu, Influence of fluorine on the structure and photocatalytic activity of TiO2 film prepared in tungstate-electrolyte via micro-arc oxidation, J. Alloys Compd., 482 (2009) 476-481.

[23] M.R. Bayati, A.Z. Moshfegh, F. Golestani-Fard, Effect of electrical parameters on morphology, chemical composition, and photoactivity of the nano-porous titania layers synthesized by pulse-microarc oxidation, Electrochim. Acta, 55 (2010) 2760-2766.

[24] M.R. Bayati, A.Z. Moshfegh, F. Golestani-Fard, In situ growth of vanadia–titania nano/micro-porous layers with enhanced photocatalytic performance by micro-arc oxidation, Electrochim. Acta, 55 (2010) 3093-3102.

[25] M.R. Bayati, A.Z. Moshfegh, F. Golestani-Fard, R. Molaei, (WO3)x–(TiO2)1–x nano-structured porous catalysts grown by micro-arc oxidation method: Characterization and formation mechanism, Mater. Chem. Phys., 124 (2010) 203-207.

[26] S. Stojadinović, N. Tadić, N. Radić, B. Stojadinović, B. Grbić, R. Vasilić, Synthesis and characterization of Al2O3/ZnO coatings formed by plasma electrolytic oxidation, Surf. Coat. Technol., 276 (2015) 573-579.

[27] S. Stojadinović, N. Radić, R. Vasilić, M. Petković, P. Stefanov, L. Zeković, B. Grbić, Photocatalytic properties of TiO2/WO3 coatings formed by plasma electrolytic oxidation of titanium in 12-tungstosilicic acid, Applied Catalysis B: Environmental, 126 (2012) 334-341.

[28] S. Stojadinović, N. Radić, B. Grbić, S. Maletić, P. Stefanov, A. Pačevski, R. Vasilić, Structural, photoluminescent and photocatalytic properties of TiO2:Eu3+ coatings formed by plasma electrolytic oxidation, Appl. Surf. Sci., 370 (2016) 218-228.

[29] M. Babaei, C. Dehghanian, M. Babaei, Electrochemical assessment of characteristics and corrosion behavior of Zr-containing coatings formed on titanium by plasma electrolytic oxidation, Surf. Coat. Technol., 279 (2015) 79-91.

[30] R.O. Hussein, X. Nie, D.O. Northwood, A. Yerokhin, A. Matthews, Spectroscopic study of electrolytic plasma and discharging behaviour during the plasma electrolytic oxidation (PEO) process, J. Phys. D: Appl. Phys., 43 (2010) 105203.

[31] M. Kosmulski, The Significance of the Points of Zero Charge of Zirconium (Hydr)Oxide Reported in the Literature, J. Dispersion Sci. Technol., 23 (2002) 529-538.

[32] Y. Yu, P. Zhang, Y. Kuang, Y. Ding, J. Yao, J. Xu, Y. Cao, Adjustment and Control of Energy Levels for TiO2–N/ZrO2–xNx with Enhanced Visible Light Photocatalytic Activity, The Journal of Physical Chemistry C, 118 (2014) 20982-20988.

[33] M. Li, X. Li, G. Jiang, G. He, Hierarchically macro–mesoporous ZrO2–TiO2 composites with enhanced photocatalytic activity, Ceram. Int., 41 (2015) 5749-5757.

[34] X. Pan, M.-Q. Yang, X. Fu, N. Zhang, Y.-J. Xu, Defective TiO2 with oxygen vacancies: synthesis, properties and photocatalytic applications, Nanoscale, 5 (2013) 3601-3614.

[35] S. Husain, L.A. Alkhtaby, E. Giorgetti, A. Zoppi, M. Muniz Miranda, Investigation of the role of iron doping on the structural, optical and photoluminescence properties of sol–gel derived TiO2 nanoparticles, J. Lumin., 172 (2016) 258-263.

[36] D.D. Macdonald, Reflections on the history of electrochemical impedance spectroscopy, Electrochim. Acta, 51 (2006) 1376-1388.

[37] L.V. Taveira, A.A. Sagüés, J.M. Macak, P. Schmuki, Impedance Behavior of TiO2 Nanotubes Formed by Anodization in NaF Electrolytes, J. Electrochem. Soc., 155 (2008) C293-C302.

[38] N. Baram, Y. Ein-Eli, Electrochemical Impedance Spectroscopy of Porous TiO2 for Photocatalytic Applications, The Journal of Physical Chemistry C, 114 (2010) 9781-9790.

[39] Y. Barsukov, J.R. Macdonald, Electrochemical Impedance Spectroscopy, Characterization of Materials, John Wiley & Sons, Inc.2002.

[40] I. Herraiz-Cardona, E. Ortega, V. Pérez-Herranz, Impedance study of hydrogen evolution on Ni/Zn and Ni–Co/Zn stainless steel based electrodeposits, Electrochim. Acta, 56 (2011) 1308-1315.

[41] J.-B. Jorcin, M.E. Orazem, N. Pébère, B. Tribollet, CPE analysis by local electrochemical impedance spectroscopy, Electrochim. Acta, 51 (2006) 1473-1479.

[42] H. Yang, X. Guo, G. Wu, W. Ding, N. Birbilis, Electrodeposition of chemically and mechanically protective Al-coatings on AZ91D Mg alloy, Corros. Sci., 53 (2011) 381-387.

[43] P. Córdoba-Torres, T.J. Mesquita, R.P. Nogueira, Toward a better characterization of constant-phase element behavior on disk electrodes from direct impedance analysis: Methodological considerations and mass transport effects, Electrochim. Acta, 92 (2013) 323-334.

[44] C.H. Hsu, F. Mansfeld, Technical Note: Concerning the Conversion of the Constant Phase Element Parameter Y0 into a Capacitance, Corrosion, 57 (2001) 747-748.

[45] V. Afshari, C. Dehghanian, Inhibitor effect of sodium benzoate on the corrosion behavior of nanocrystalline pure iron metal in near-neutral aqueous solutions, J. Solid State Electrochem., 14 (2010) 1855-1861.

[46] B. Hirschorn, M.E. Orazem, B. Tribollet, V. Vivier, I. Frateur, M. Musiani, Determination of effective capacitance and film thickness from constant-phase-element parameters, Electrochim. Acta, 55 (2010) 6218-6227.

[47] Q. Wang, S. Ito, M. Grätzel, F. Fabregat-Santiago, I. Mora-Seró, J. Bisquert, T. Bessho, H. Imai, Characteristics of High Efficiency Dye-Sensitized Solar Cells, The Journal of Physical Chemistry B, 110 (2006) 25210-25221.

[48] H. Zhang, X. Lv, Y. Li, Y. Wang, J. Li, P25-Graphene Composite as a High Performance Photocatalyst, ACS Nano, 4 (2010) 380-386.

[49] B. Neppolian, Q. Wang, H. Yamashita, H. Choi, Synthesis and characterization of ZrO2–TiO2 binary oxide semiconductor nanoparticles: Application and interparticle electron transfer process, Applied Catalysis A: General, 333 (2007) 264-271.

[50] H. Salavati, N. Tavakkoli, M. Hosseinpoor, Preparation and characterization of polyphosphotungstate/ZrO2 nanocomposite and their sonocatalytic and photocatalytic activity under UV light illumination, Ultrason. Sonochem., 19 (2012) 546-553.

[51] V.K. Gupta, R. Jain, A. Mittal, M. Mathur, S. Sikarwar, Photochemical degradation of the hazardous dye Safranin-T using TiO2 catalyst, J. Colloid Interface Sci., 309 (2007) 464-469.

Figure captions

Fig. 1. Surface morphologies of layers prepared at (a, d, and g) D=30%, (b, e, and h) D=50% and (c, f and i) D=70% in (a, b and c) 0 g/l, (d, e and f) 2 g/l, and (g, h and i) 4 g/l sodium zirconate containing electrolyte.

Fig. 2. XRD patterns of the layers produced at different electrolytes under various duty cycles.

Fig. 3. UV-vis diffuse reflectance spectra (a) of pure TiO_2 and TiO_2-ZrO_2 composite layers synthesized in electrolytes with different concentration and (b) their corresponding plots of $(A/\lambda)^{1/m}$ vs. $(1/\lambda)$.

Fig. 4. Photoluminescence spectra of the layers produced at different electrolytes and various duty cycles.

Fig. 5. Complex and Bode diagrams of MAO layers formed at different duty cycles in (a and b) electrolyte A2 and (c and d) electrolyte A4.

Fig. 6. Equivalent circuits to model behavior of MAO layers formed in (a) electrolyte A2 and (b) electrolyte A4.

Fig. 7. The kinetic of photocatalytic degradation of MB with (a) pure TiO_2 layer and other photocatalyst layers formed at D=50%. Effect of duty cycle on the photocatalytic activity of the composite layers formed in (b) electrolyte A2 and (c) electrolyte A4.

Fig. 8. Time dependency of photocatalytic activity of (a) pure TiO_2 layer and other photocatalyst layers formed at D=50%. Effect of duty cycle on the photocatalytic activity of the composite layers formed in (b) electrolyte A2 and (c) electrolyte A4.

Table captions

Table 1. The composition, pH and conductivity of the electrolyte systems used for MAO process with their respective identification codes.

Table 2. The elemental composition on the surface of the layers by EDS analyses.

Table 3. Fitting values of the equivalent circuit elements.

Table 4. Calculated C_{dl} and C_i from the best-fit estimates of equivalent circuit parameters obtained from the impedance measurements of the layers in $NaSO_4$ solution.

Table 5. Photo-catalytic reaction rate constants (k) for the pure TiO_2 and the TiO_2-ZrO_2 composite layers fabricated at different duty cycles.
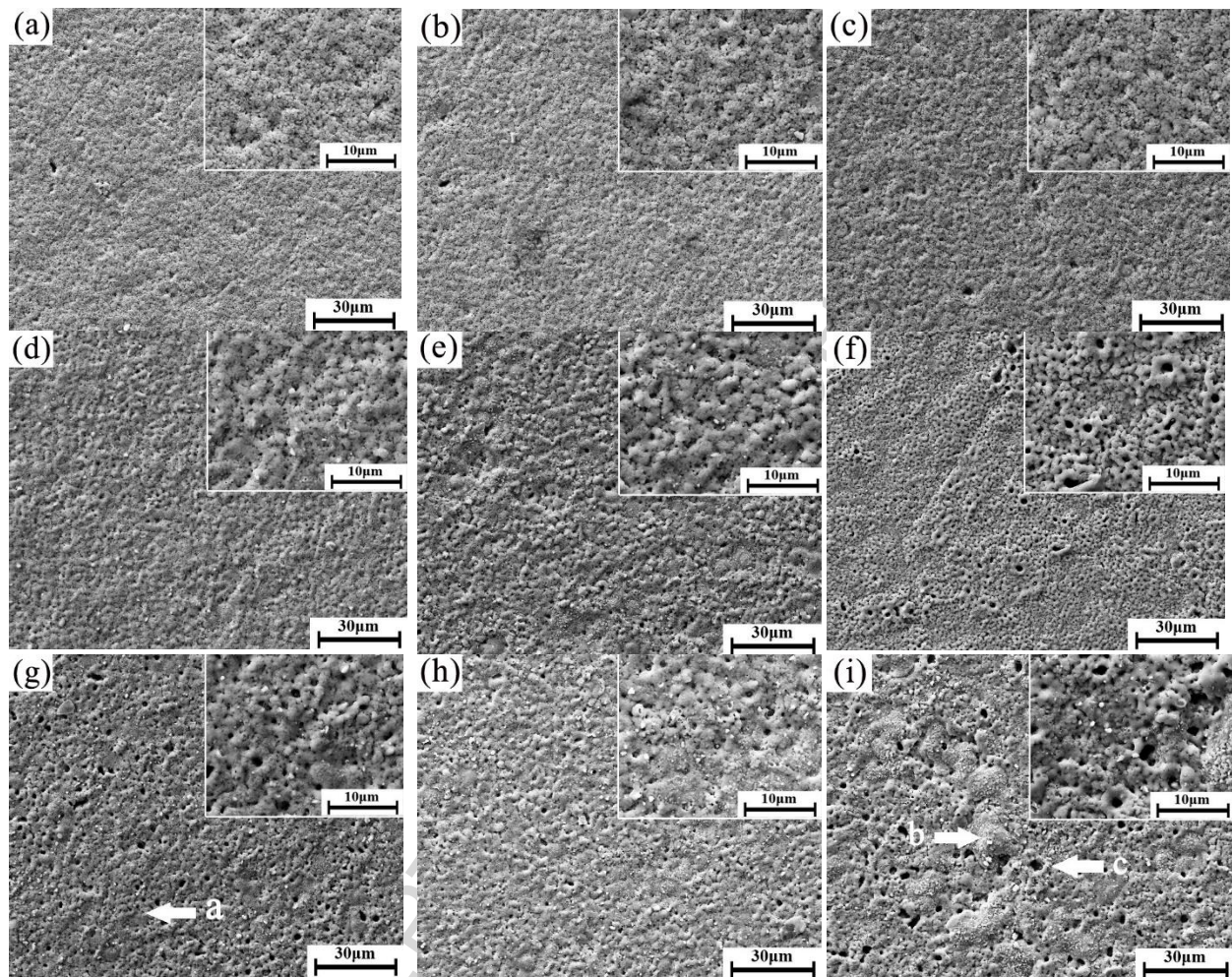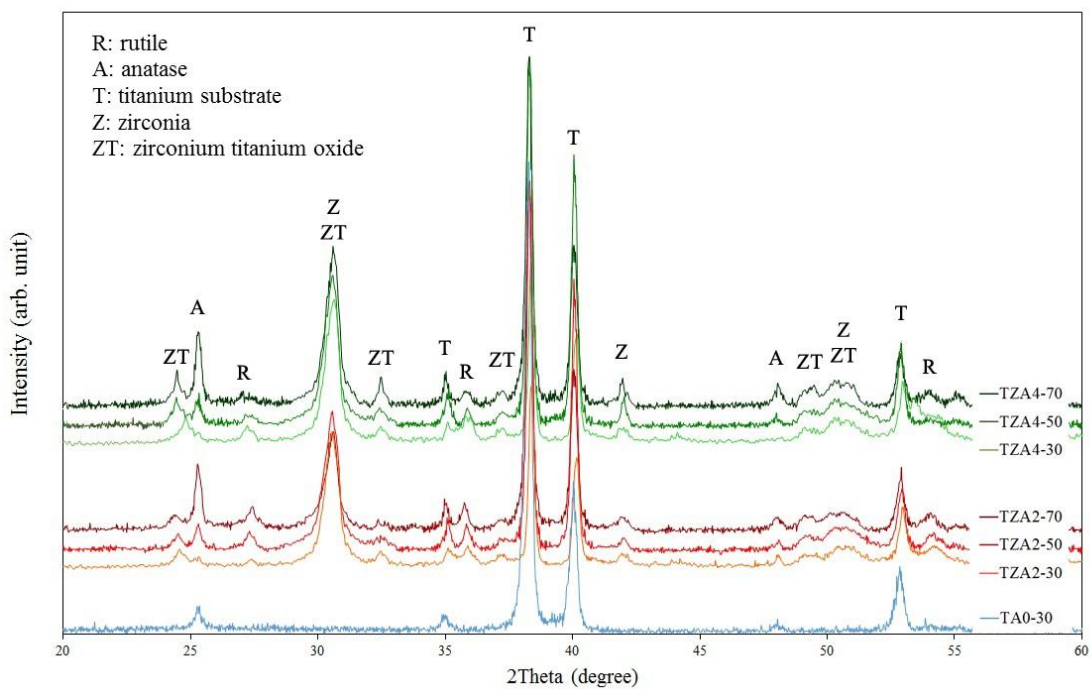
Fig. 1

Fig. 2

Fig. 3
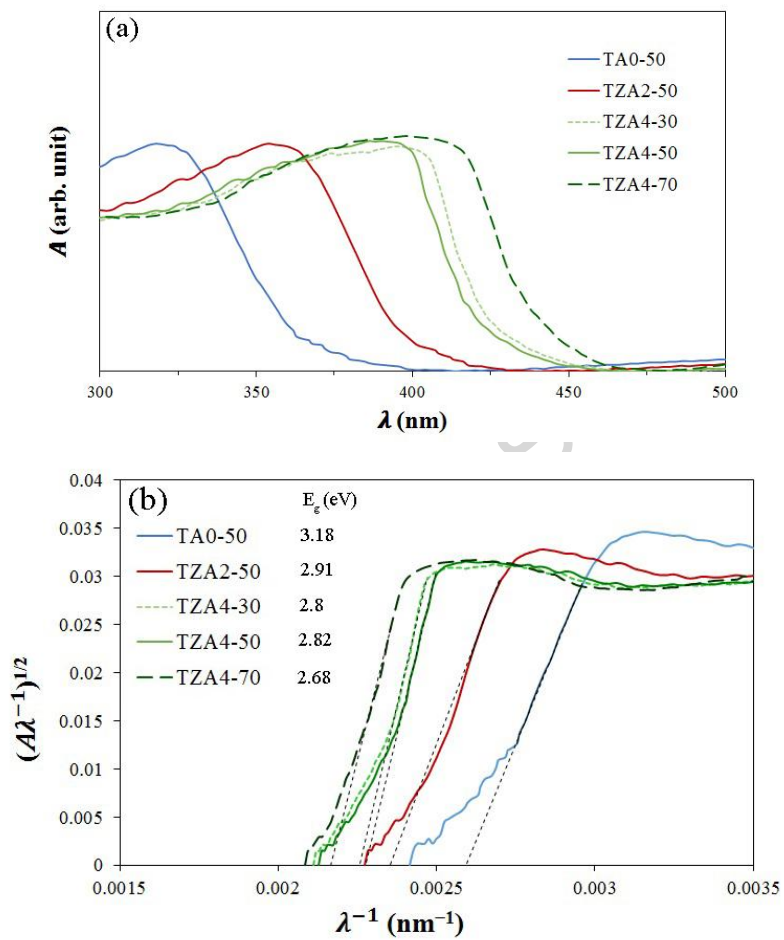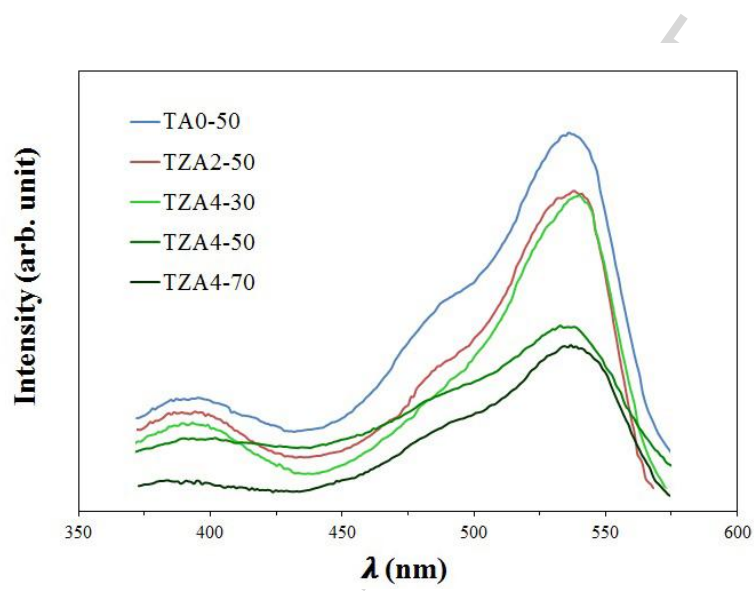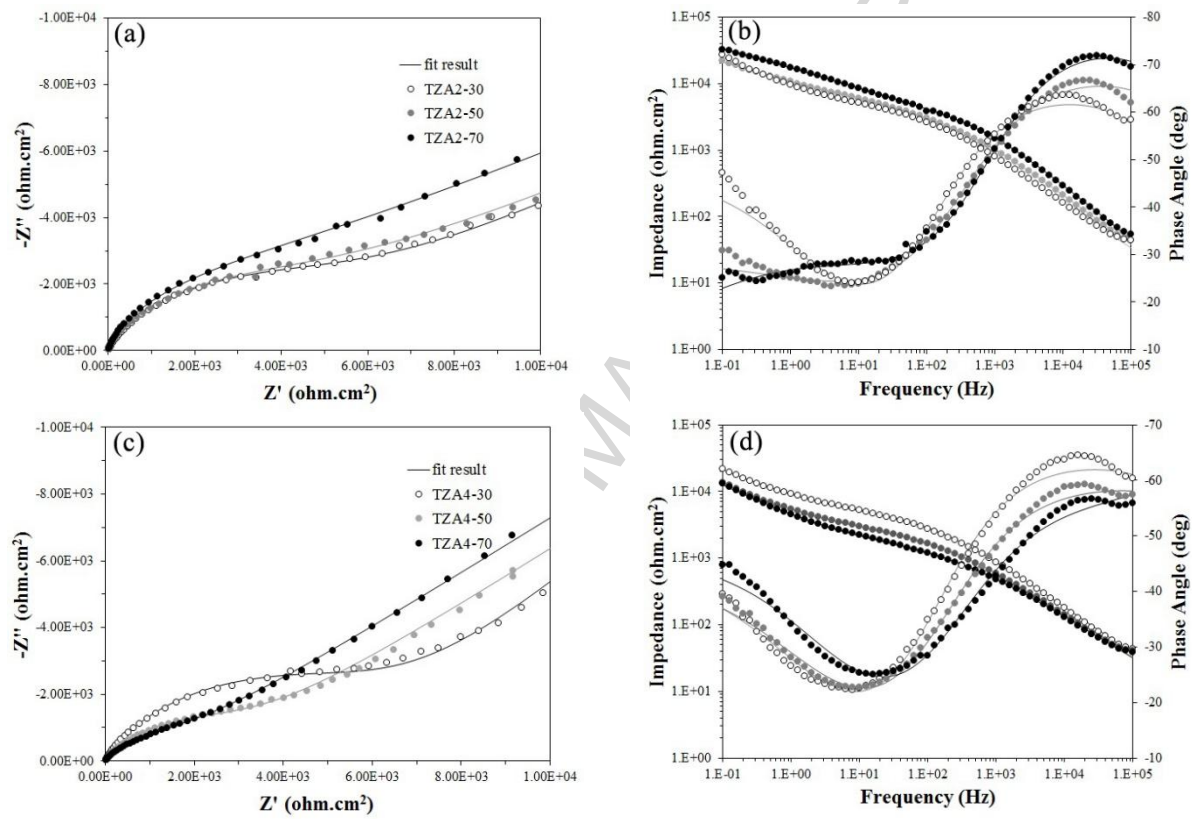
Fig. 4

Fig. 5
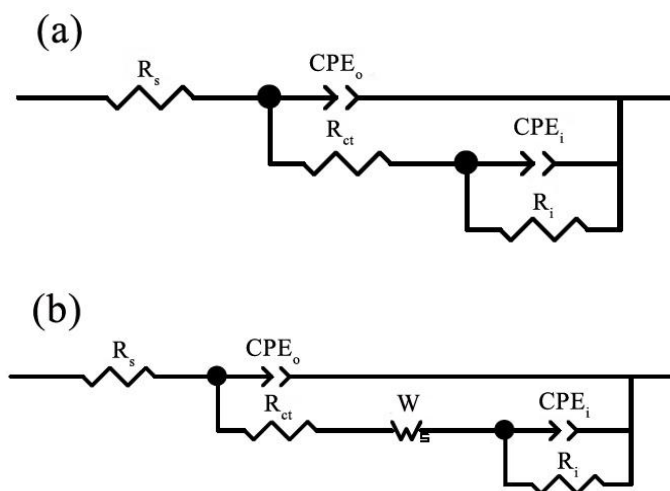
Fig. 6
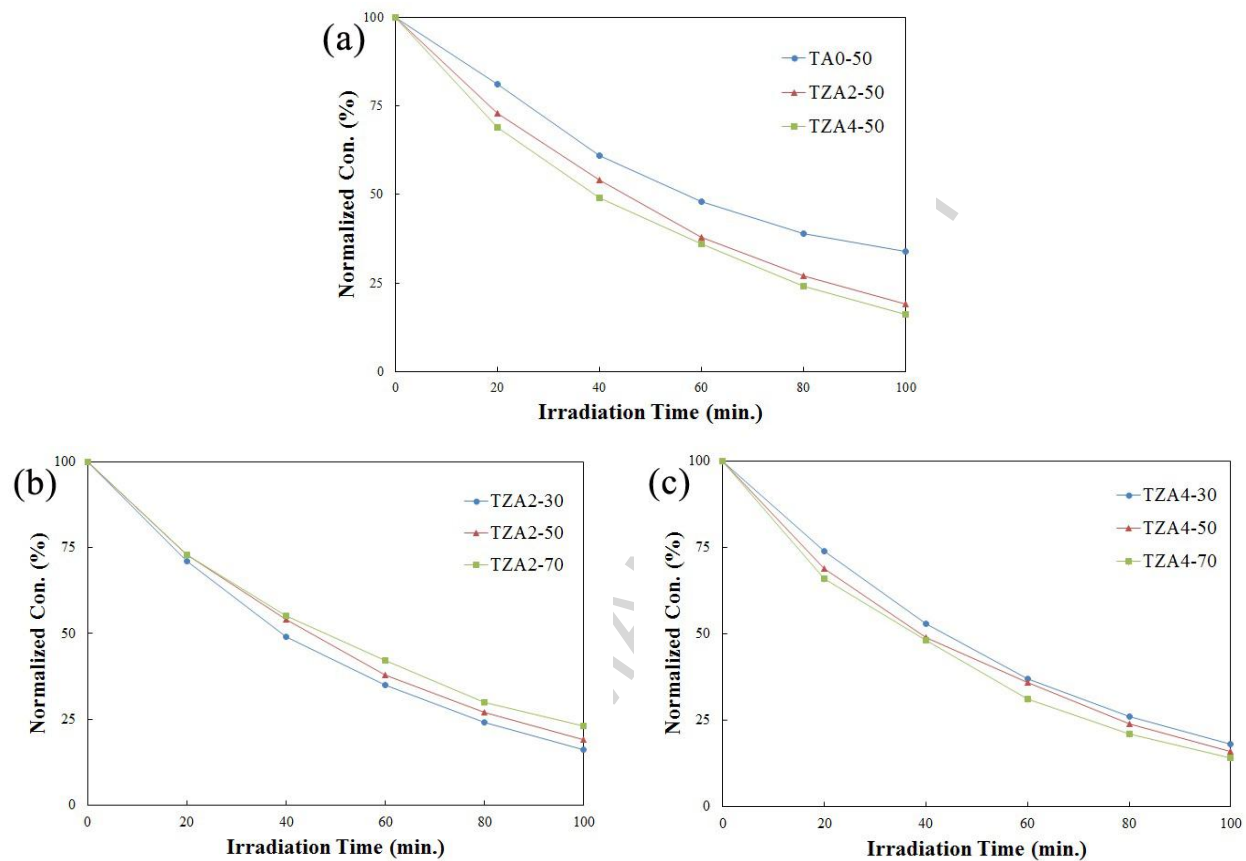
Fig. 7

Fig. 8

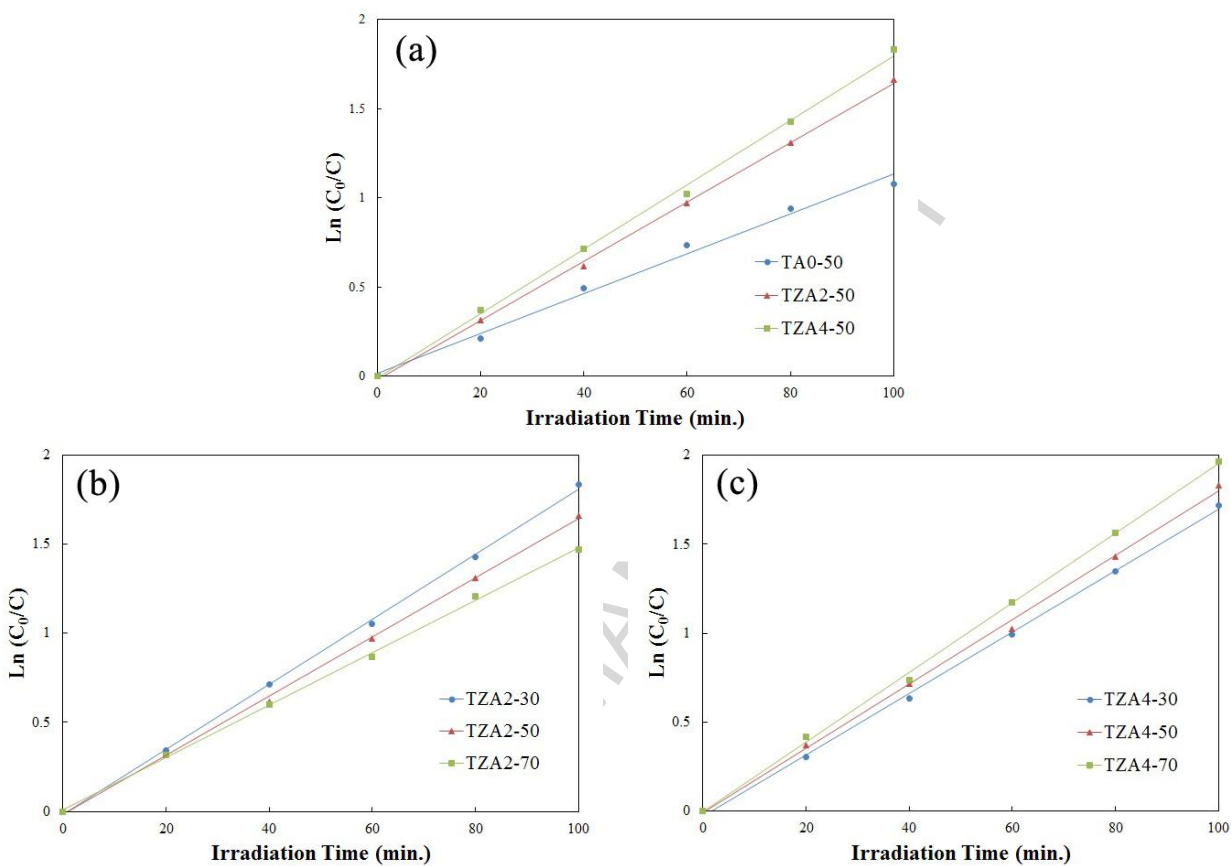**Table 1.** The composition, pH and conductivity of the electrolyte systems used for PEO process with their respective identification codes.

Electrolyte code	Electrolyte composition (g/l)	pH	Conductivity κ (mS/cm)
A0	2 g NaH_2PO_4	6.1	8.7
A2	2 g NaH_2PO_4+2 g Na_2ZrO_3+1 g Na_2SiO_3	7.2	11.4
A4	2 g NaH_2PO_4+4 g Na_2ZrO_3+1 g Na_2SiO_3	8.6	13.1

Table 2. The elemental composition on the surface of the layers by EDS analyses.

	TZA2-30	TZA2-50	TZA2-70	TZA4-30	TZA4-50	TZA4-70
Ti (wt%)	48.29	49.87	52.34	44.21	43.64	43.78
Zr (wt%)	7.73	3.91	3.03	7.46	7.92	12.51
O (wt%)	31.12	31.56	31.63	33.88	34.52	27.94
C (wt%)	4.48	7.12	5.44	5.45	3.01	5.11
P (wt%)	7.11	6.6	6.89	7.78	8.43	8.74
Si (wt%)	1.27	0.94	0.67	1.22	2.48	1.92

Table 3. Fitting values of the equivalent circuit elements.

	TZA2-30	TZA2-50	TZA2-70	TZA4-30	TZA4-50	TZA4-70
R_s (Ω cm^2)	6.04	3.21	5.13	4.01	0.62	0.03
R_{ct} (Ω cm^2)	3264	5451	6983	6335	3270	2235
R_i (Ω cm^2)	6.17×10^4	7.36×10^4	1.2×10^5	1.15×10^5	5.18×10^4	5.38×0^4
CPE_o(T)	1.69×10^{-6}	6.58×10^{-7}	2.22×10^{-7}	1.38×10^{-6}	2.94×10^{-6}	5.99×10^{-6}
CPE_o(P)	0.74	0.79	0.86	0.84	0.76	0.73
CPE_i(T)	5.19×10^{-5}	4.29×10^{-5}	2.17×10^{-5}	4.08×10^{-5}	5.86×10^{-5}	6.06×10^{-5}
CPE_i(P)	0.33	0.34	0.34	0.52	0.45	0.43
W_s(T)	-	-	-	0.39	0.34	0.33
W_s(P)	-	-	-	0.28	0.31	0.30
W_s(R)	-	-	-	5910	3730	2473

Table 4. Calculated C_{dl} and C_i from the best-fit estimates of equivalent circuit parameters obtained

from the impedance measurements of the layers in NaSO$_4$ solution.

	TZA2-30	TZA2-50	TZA2-70	TZA4-30	TZA4-50	TZA4-70
C$_{dl}$ (µFcm^{-2})	0.27	0.14	0.07	0.56	0.68	1.21
C$_i$ (Fcm^{-2})	5.49×10^{-4}	3.99×10^{-4}	1.39×10^{-4}	1.69×10^{-4}	2.27×10^{-4}	2.90×10^{-4}

Table 5. Photo-catalytic reaction rate constants (k) for the pure TiO_2 and the TiO_2-ZrO_2 composite layers fabricated at different duty cycles.

	TA0-50	TZA2-30	TZA2-50	TZA2-70	TZA4-30	TZA4-50	TZA4-70
Average k, (min^{-1}) $\times 10^{-3}$	11.2	18.2	16.6	14.7	17.2	18.1	19.6

Highlights

- TiO_2-ZrO_2 composite layers are formed by micro arc oxidation (MAO).

- The microdischarge regime is influenced by duty dycle.

- Zr^{4+} ions replace Ti^{4+} ions and form impurity levels, which could prolong carrier lifetime.

- The synthesized composite layers show enhanced photo-catalytic activity.

- Photocatalytic activity of layers is related to morphology and elemental composition.